ADVANCED FUNCTIONAL MATERIALS
www.afm-journal.de

In Situ Thermolysis of a Ni Salt on Amorphous Carbon and Graphene Oxide Substrates

*Mahmound Tamadoni Saray, Vitaliy Yurkiv, and Reza Shahbazian-Yassar**

Understanding the thermal decomposition of metal salt precursors on carbon structures is essential for the controlled synthesis of metal-decorated carbon nanomaterials. Here, the thermolysis of a Ni precursor salt, $NiCl_2{\cdot}6H_2O$, on amorphous carbon (a-C) and graphene oxide (GO) substrates is explored using in situ transmission electron microscopy. Thermal decomposition of $NiCl_2{\cdot}6H_2O$ on GO occurs at higher temperatures and slower kinetics than on a-C substrate. This is correlated to a higher activation barrier for Cl_2 removal calculated by the density functional theory, strong Ni-GO interaction, high-density oxygen functional groups, defects, and weak van der Waals using GO substrate. The thermolysis of $NiCl_2{\cdot}6H_2O$ proceeds via multistep decomposition stages into the formation of Ni nanoparticles with significant differences in their size and distribution depending on the substrate. Using GO substrates leads to nanoparticles with 500% smaller average sizes and higher thermal stability than a-C substrate. Ni nanoparticles showcase the *fcc* crystal structure, and no size effect on the stability of the crystal structure is observed. These findings demonstrate the significant role of carbon substrate on nanoparticle formation and growth during the thermolysis of carbon–metal heterostructures. This opens new venues to engineer stable, supported catalysts and new carbon-based sensors and filtering devices.

1. Introduction

Generally, thermolysis is a thermochemical decomposition where the precursor decomposition in a solid state or solution phase occurs at high temperatures to break the chemical bonds in order to initiate new chemical compounds in which the rearrangement of constituent atoms determines nanocrystal growth and formation.[1,2] This process has been employed to synthesize a wide range of nanostructured organic and inorganic materials including metals, metal oxides, metal sulfides, non-oxide ceramics, and carbon materials.[3] Since the thermolysis process involves many chemical and physical transformations over the synthesis time span, in situ characterization methods are needed to clarify the pathway of reaction mechanisms or their correlation with the substrate. However, few in situ measurements have investigated the thermolysis process and the most noticeable ones include in situ Fourier-transform infrared spectroscopy and in situ X-ray powder diffraction (XRD),[4,5] in situ variable-temperature small angle X-ray scattering,[6] and in situ transmission electron microscopy (TEM).[7]

In situ scanning/transmission electron microscopy (S/TEM) techniques have been used to elucidate atomic insights into thermolysis-driven nanomaterials growth/formation. Therefore, having a fundamental understanding of solid-state transformation on the nanoscale could provide guidelines for precise control of the synthesis parameters. For example, Sang et al.[8] utilized in situ S/TEM on the growth of MoS_2 from thermolysis of ammonium thiomolybdate $(NH_4)_2MoS_4$ precursor with different precursor thicknesses, growth substrate , and annealing temperatures. They proposed the growth mechanism as the formation of short-range order MoS_2 nanograins from amorphous salt decomposition, followed by grain coalescence via orientation attachment and grain boundary movement at higher temperatures. Fei et al.[9] distinguished two formation stages of MoS_2 flakes during the thermal decomposition of solid ammonium thiomolybdates on amorphous silicon nitride substrate using in situ TEM. They observed layer-by-layer growth of vertical MoS_2 at low temperatures followed by horizontal orientation at higher temperatures due to the energy minimization of the MoS_2 and Si_3N_4 system during crystal structure growth. Recently, Gavhane et al.[7] investigated the growth dynamics of tungsten disulfide (WS_2) layers through thermolysis of an amorphous single solid-state ammonium tetrathiotungstate, $(NH_4)_2WS_4$ precursor on silicon nitride membrane and metal substrates using in situ TEM. They reported vertical growth of WS_2 layers at thick precursor regions while horizontal crystallization of WS_2 layers happened at thin precursor areas.

M. Tamadoni Saray, R. Shahbazian-Yassar
Department of Mechanical and Industrial Engineering
University of Illinois Chicago
Chicago, IL 60607, USA
E-mail: rsyassar@uic.edu
V. Yurkiv
Department of Aerospace and Mechanical Engineering
University of Arizona
Tucson, AZ 85721, USA
The ORCID identification number(s) for the author(s) of this article can be found under https://doi.org/10.1002/adfm.202213747.

DOI: 10.1002/adfm.202213747

Despite the vast interest in understanding the thermolysis of metal salts, in situ studies of metal salt/substrate evolution during exposure to high-temperature cycles have been scarce. Here, we used in situ heating in an aberration-corrected transmission electron microscopy (TEM) to study the thermolysis of Ni salt on graphene oxide (GO) nanosheets and amorphous carbon (a-C) substrates via a heating/cooling approach. We observed that heating led to metallic Ni nanoparticles (NPs) with face-centered cubic (*fcc*-Ni) crystal structures on both carbon substrates. Using GO substrate resulted in more stable metal nanoparticles with small size (≈8 nm) and random distribution, while large nanoparticles (≈38 nm) with bimodal distribution formed on a-C support.

2. Results and Discussion

In this work, we performed in situ TEM studies to synthesize nickel nanoparticles decorated on reduced graphene oxide (rGO) nanosheets (Ni/rGO) and amorphous carbon (Ni/a-C). **Figure 1** schematically illustrates the experimental approach for Ni/rGO and Ni/a-C systems. Here, we utilized an in situ heating TEM holder with the capability for placing silicon microfabricated chips comprised of silicon carbide (SiC) heating membrane with nine 8 µm holes in the center covered with amorphous holey carbon for sample support. Heating occurs when an electrical current is forced across the conductive membrane (Figure 1a). As shown in Figure 1b, the applied heating profile for in situ experiment systems is performed according to the heating and cooling rate of 10 °C sec^{-1} for Ni/rGO and Ni/a-C synthesis. Ni precursor ($NiCl_2.6H_2O$) formed a thin film deposit on graphene oxide (GO) (step I, Figure 1c). Subsequently, by applying in situ heating, the $NiCl_2.6H_2O$ precursor is expected to decompose into Ni atoms and form volatile gas species along with GO reduction, as shown in step II in Figure 1c. Eventually, Ni atoms can nucleate as Ni nanoparticles (step III, Figure 1c). Similarly, for Ni/a-C case, the Ni precursor solution was deposited on a-C film directly forming $NiCl_2.6H_2O$ droplets (step I, Figure 1d). Next, the droplets thermally decomposed into Ni atoms and various volatile gas molecules by in situ heating (step II in Figure 1d) followed by Ni nanoparticle formation (step III in Figure 1d).

Before the start of the heating experiments, we assessed the Ni salt/carbon substrate deposition on the heating chip via TEM and energy-filtered TEM (EFTEM). Figure 1e provides a low magnification TEM image of the $NiCl_2.6H_2O$ /GO mixture positioned in the holey region of carbon film supported on a silicon carbide heating microchip. Interestingly, a thin layer of $NiCl_2.6H_2O$ film is formed on the GO substrate (Figure 1f). This can be attributed to the presence of surface functional groups of GO nanosheets, which have strong chemisorption capacity to metal ions and form metal-ion-modified GO films.[10–12] In contrast, the Ni salt solution form large droplets (>500 nm) on amorphous carbon support rather than forming a thin film as we observed using GO nanosheets (Figure 1g,h). This is caused by the hydrophobic nature of amorphous carbon.[13] The higher magnification TEM images present GO and a-C surface decoration with small nickel chloride hexahydrate, $NiCl_2.6H_2O$ nanocrystals (10–20 nm) with lattice fringes of 5.68 and 5.42 A corresponding to (001) and (110) planes of $NiCl_2.6H2O$ (Figure S1a,c, Supporting Information). Furthermore, selected area electron diffraction (SAED) patterns of the as-deposited Ni salt precursor in Figure S1b,d (Supporting Information) confirm the monoclinic crystal structure of $NiCl_2.6H_2O$ (space group: *C*2/*m*) forming on GO nanosheets and a-C upon drop casting/drying of initial diluted solution. Furthermore, EFTEM was performed to examine the elemental distribution within the deposited nickel salt on an a-C substrate. This technique

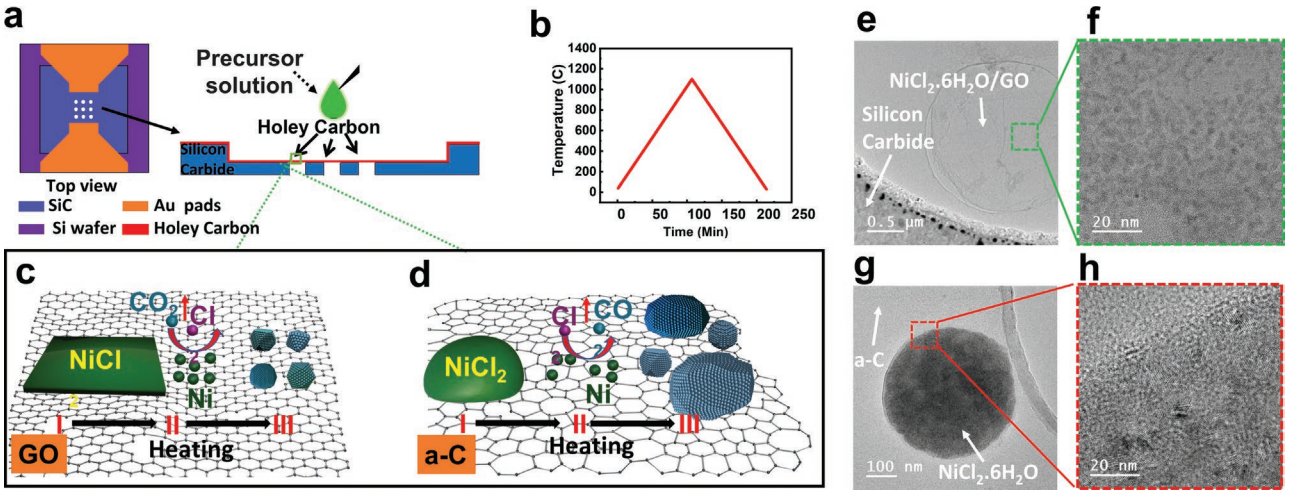

Figure 1. Schematic illustration of the formation of Ni NPs on rGO nanosheet and a-C substrate via heating procedures. a) Representation of electrical biasing in situ heating TEM system, microchip equipped with a heater to study Ni NPs formation. b) Graphical heating profile applied for in situ experiment. c) The sequential evolution of the $NiCl_2.6H_2O$ precursor to Ni NPs through thermal decomposition: I: solid precursor $NiCl_2.6H_2O$ thin film formed on GO substrate; II: upon heating precursor salt and GO transformed into Ni atoms with by-products of gaseous species; III: formation of Ni nanoparticles. d) The sequential evolution of the $NiCl_2.6H_2O$ to Ni NPs formation on the amorphous carbon (a-C) support via thermal decomposition, I: $NiCl_2.6H_2O$ droplet formed on a-C upon drop casting; II: in situ heating led to thermal decomposition of precursor salt into Ni atoms and released gasses; III: Ni nanoparticles formed on a-C substrates, respectively. e,f) low magnification TEM images of $NiCl_2.6H_2O$ salt precursor forming a thin film on GO. g,h) low magnification TEM images of Ni salt precursor forming as droplets on a-C.

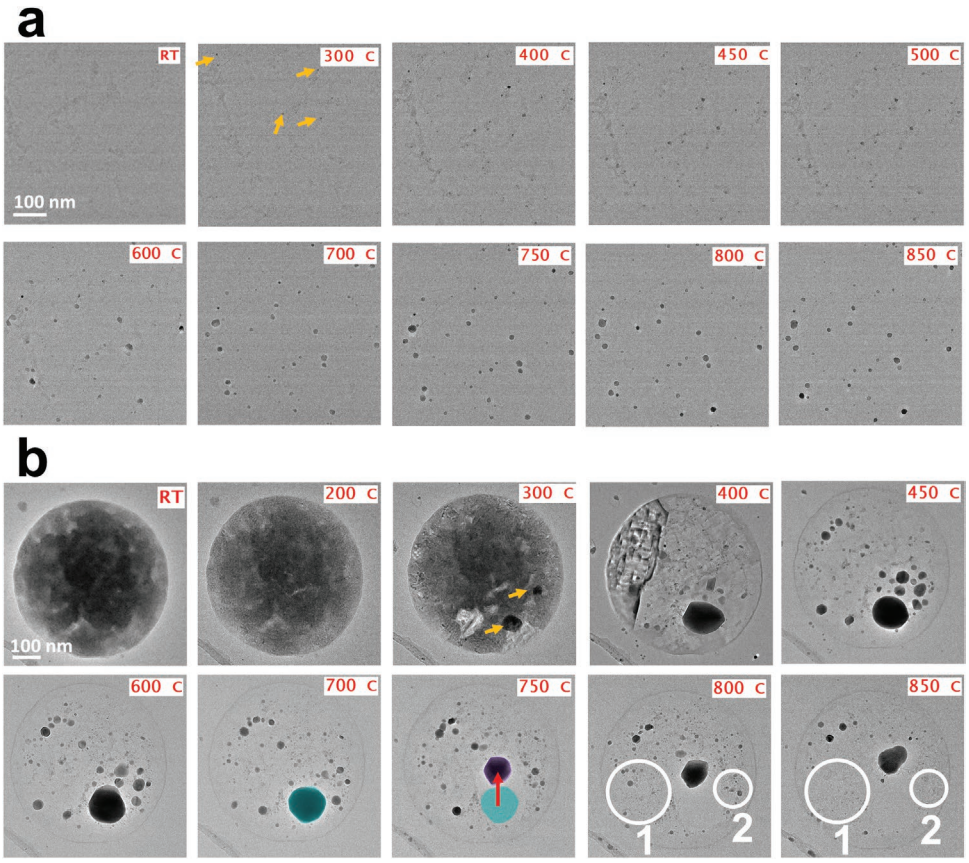

Figure 2. In situ time-resolved TEM image series depicting the formation of Ni nanoparticles on a) GO, and b) amorphous carbon (a-C) during heating. Some of the nucleated NPs are marked with yellow arrows. In (b), the green shade at 700 °C corresponds to the initial position of a large particle, and the red arrow shows the particle displacement at 750 °C on a-C support. White circles 1 and 2 show examples of Ni NPs disappearances on a-C substrate above 800 °C.

provides rapid elemental mapping for light elements and intensive beam-sensitive materials. Figure S2a,b (Supporting Information) presents an elastic TEM image of the $NiCl_2.6H_2O$ and the corresponding elemental maps. Uniform distribution of Ni L-edge, Cl-L-edge, and O K-edge was directly observed via EFTEM maps, confirming that nickel chloride deposition was in hydrated form.

The decomposition of metal salt precursor solution on carbon substrates (GO, a-C) upon heating (10 °C min^{-1}) was studied via time-resolved TEM imaging (**Figure 2**). As depicted in Figure 2a, the $NiCl_2.6H_2O$ thin film on GO remains stable up to 300 °C in which we could observe the nanoparticles nucleation stage (marked with yellow arrows). This is correlated to the $NiCl_2$ decomposition temperature range measured by TGA.[14,15] As the heating temperature increases to the reductive temperature of $NiCl_2$ (400 °C) in which pure metal is prepared, more nanoparticles are formed, and the size of particles increases up to 600 °C.[16] It could be seen that the formed nanoparticles are stable and separated without distinguishable particle migration/coalescence up to 850 °C. In addition, as it will be discussed in the following, the GO substrate transforms to reduced GO (rGO) at temperatures exceeding 300 °C.[17,18] These results confirmed the excellent thermal stability of NPs formed on the rGO within the operating temperature cycle. This could be assigned to strong metal-rGO interactions and possible chemical bonding of Ni—C atoms that anchor them to the surface.[19] Also, the presence of defective sites of rGO increases diffusion barriers for atom migration.[20] Therefore, the dispersed NPs pinned and stayed stable up to 850 °C, and we did not observe noticeable aggregation or coalescence of nearby nanoparticles.

We applied the same heating cycle for Ni salt precursor on a-C substrate and captured the dynamic of Ni salt decomposition and nanoparticles formation upon heating. Figure 2b illustrates the evolution of deposited $NiCl_2.6H_2O$ on a-C upon heating to 850 °C at 10 °C min^{-1} heating ramps. During heating, we observed thermal decomposition of the metal salt precursor started at ≈300 °C and progressively continued up to 400 °C. Also, one might note that the disappearance of the precursor phase is corroborated by the emergence of nanoparticles as appeared by their darker image contrast. By 450 °C, the entire precursor microdroplet converted into presumably Ni nanoparticles. Additionally, by further increasing the temperature, the growth of Ni nanoparticles continued. These particles are stable up to 550 °C. However, particle migration and coalescence of close particles are captured at higher temperatures. We noted that above 700 °C, a large particle (Figure 2b, $T = 750$ °C) was displaced on the substrate and shrank in size (marked with

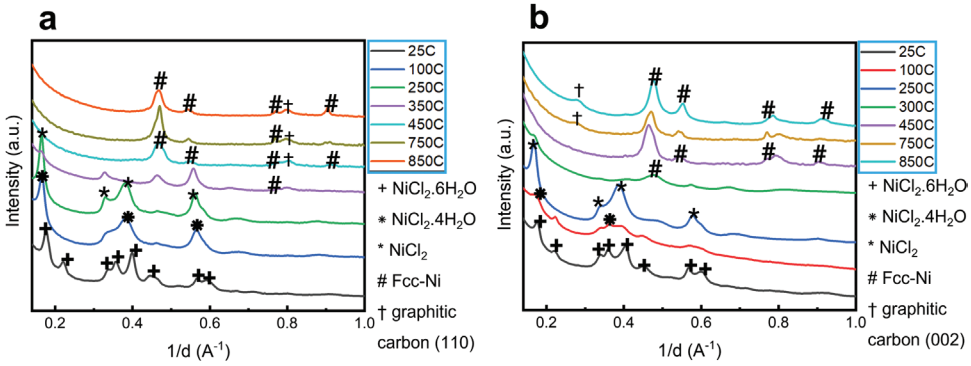

Figure 3. The intensity line profiles derived from the temperature series SAED patterns from thermolysis of a) $NiCl_2.6H_2O$/GO, and b) $NiCl_2.6H_2O$/a-C.

a green circle). This can be correlated to weaker Ni- graphitized carbon support interaction at elevated temperatures (700 °C), facilitating NP mobility and particle growth on carbon support which we discuss later. After 800 °C, the number of the small-sized particles decreases with the increase in temperature (highlighted white circle regions 1, 2).

The disappearance of nanoparticles can be correlated to two possible mechanisms. One possibility is the redispersion of large nanoparticles into clusters or single atoms species bonded to carbon substrates. Because the electronic configuration of nickel favors covalent bonding with carbon substrates, the elevated temperature will enhance Ni-carbon bonding.[19] A similar observation has been reported by Huang et al. reported the strong covalent bonding between Pt atoms and graphene edge planes at high temperatures, which led to the conversion of nanoparticles into stable single atoms on the substrate.[20] Another possibility is the reduction in the evaporation temperature of metal nanoparticles due to higher vapor pressure and surface tension compared to their bulk counterpart.[21,22] This is supported by a recent study revealing the strong correlation between the melting point (T_{mp}) and the size of Ni nanoparticles, where nanoparticles with small diameters could form a liquid phase at temperatures well below the melting temperature of bulk Ni (1450 °C).[23] We should emphasize that factors including particle size, vacuum pressure, and electron dose can also be a factor here and would need to be studied in more details.

Multiple-step structural evolution of precursor occurs at higher temperatures with slower kinetics on GO substrate than a-C. We performed experiments involving SAED and high-resolution in situ TEM experiments to clarify the role of carbon substrate on the $NiCl_2.6H_2O$ evolution. The sequential SAED of hydrated nickel salt on GO and a-C patterns during thermolysis from room temperature to 850 °C were collected to discern the structural change with temperature (Figure S3, Supporting Information). Analysis of structural data depicted multiple stages involved in the thermolysis of $NiCl_2.6H_2O$ on both substrates. The reflections from electron diffraction patterns were indexed according to their positions with increasing temperature. $NiCl_2$ decomposition into Ni on GO substrate occurs at a higher temperature than its a-C counterpart. Moreover, the line intensity profiles extracted by the rotation averaging process from the recorded SAED patterns provide structural analysis during the evolution of $NiCl_2.6H_2O$ as a function of carbon substrate (**Figure 3**a,b). The corresponding intensity profiles were compared with the simulated powder XRD of $NiCl_2.6H_2O$, $NiCl_2.4H_2O$, $NiCl_2$, NiO, and fcc-Ni to identify the structures with characteristic periodicity.

Figure 3a illustrates the diffractograms of various intermediate production of decomposition on GO substrate. The initial precursor is well-matched with monoclinic nickel chloride hexahydrate at room temperature. By increasing the temperature to 100 °C, the appearance of new peaks and shifts in peak position corresponded to $NiCl_2.4H_2O$, indicating easy removal of uncoordinated water molecules with Ni at medium temperature. Further increasing the temperature to 250 °C resulted in anhydrous nickel chloride heterogeneous mixtures. As shown in Figure S3a (Supporting Information), the faint reflections at 325 °C correspond to the anhydrous $NiCl_2$ phase. Above 350 °C and chlorine loss, new diffractions appeared, which can be identified with the formation of the *fcc*- nickel phase and rGO (110) plane as highlighted with white semicircles and red semicircles, respectively (Figure S3a, Supporting Information). On the other hand, Figure 3b illustrates intensity profiles from the thermal decomposition process of $NiCl_2.6H_2O$ on a-C. At room temperature, the intensity profile matches characteristic peaks in the simulated powder XRD from $NiCl_2.6H_2O$. By increasing the temperature, and dehydration, removing the bonded H_2O, the distinct peaks change, and the intensity profile evolves into typical $NiCl_2.4H_2O$ ≈100 °C. $NiCl_2$ appears ≈250 °C by removing the remaining structural water. Eventually, the $NiCl_2$ compound decomposes through dichlorination, is reduced into Ni, and forms nickel nanoparticles at ≈300 °C. Also, it was noted that the SAED pattern from polycrystalline fcc-Ni is the prominent feature of the decomposition of $NiCl_2$ in the case of both substrates. It is worth mentioning that the peaks intensity from Ni (111), Ni (200), Ni (220), and Ni (311) planes are more intensive above 450 °C, indicating increased crystallinity with temperature using both substrates. Furthermore, (002) and (110) graphitic carbon reflections became apparent when the heating temperature was ≈650 °C, which agrees with the reported Ni-catalytic graphitization.

Our findings demonstrated that nickel chloride is more stable on GO substrate than a-C (325 °C vs 300 °C), which we assigned to $NiCl_2$ interaction with substrates. It is established that the surface functionality of carbon materials significantly affects the metal ions' adsorption. For example, Chung.[24] reported enhancement of metal ions interaction with oxidized

carbon materials and more negative Gibbs free energy change ($\Delta G°$) for modified CNTs adsorbent compared to as-produced CNTs. Similarly, Ni cations demonstrated thermodynamically favorable and strong adsorption onto oxidized carbon nanotubes.[25] Moreover, the negative value of Gibb's free energy suggests that Ni ions' interaction with GO substrate is spontaneous and physical adsorption ($\Delta G° > -20$ KJ mol^{-1}).[26] Therefore, the presence of strong electrostatic bonding between positively charged metal ions and negatively charged sites of GO compared to a-C substrates resulted in improved thermal stability of the GO-metal complex.

In order to clarify better the $NiCl_2$ thermolysis as a function of carbon substrate, time-lapse high resolution-TEM-transmission electronn microscopy (HR-TEM) imaging was performed. We should emphasize that the preliminary experiments confirmed a negligible beam effect on the precursor at a higher dose rate (3000 e A^{-2} s^{-1}) over an extended time (Figure S4, Supporting Information). Therefore, the reduced beam irradiation dose rate during in situ experiment is low enough (300 e A^{-2} s^{-1}) to avoid any beam-induced damage to the sample so that genuine crystalline structure and atomic arrangement can be affected solely by the heating experiment. The deposited nickel salt on GO and a-C preserved its morphology upon heating to 275 and 250 °C, respectively (Figure S5, Supporting Information). **Figure 4** illustrates the evolution of $NiCl_2$ into Ni nanoparticles upon thermolysis on GO and a-C substrates under the same imaging conditions and electron dose rate of 300 e A^{-2} s^{-1}. Higher magnification TEM characterization of the precursor on GO at 300 °C shows lattice spacing 5.93°A° corresponding to $NiCl_2$ (003). This agrees with SAED observation, further confirming the removal of water of crystallization (Figure S6, Supporting Information). The $NiCl_2$ crystalline domains gradually disappeared and shrank in size with increasing temperature from 290 °C up to 330 °C, as highlighted in the crystalline regions 1–6 colored purple surroundings (Figure 4a). Eventually, at 332 °C, the $NiCl_2$ crystallites disappeared, leaving the Ni clusters, which grew to form Ni nanoparticles, as highlighted with a dashed cyan counter. On the other hand, $NiCl_2$ crystalline domains marked with purple color (1–6) at 275 °C in Figure 4b gradually reduced in size with temperature up to 298 °C, and newly formed Ni nanoparticles appeared at 305 °C (dashed cyan counter). Regarding the transformation of the material from precursor $NiCl_2.6H_2O$ to Ni nanoparticles, SAED and HR-TEM results revealed two distinct features of nickel salt decomposition of GO and a-C: (1) thermal decomposition temperature of nickel chloride on GO occurs at a higher temperature than a-C (332 °C versus 305 °C), and (2) the $NiCl_2$ thermal decomposition dynamics are slower on the GO substrate (ΔT = 42 °C) compared to a-C (ΔT = 35 °C).The in situ low-angle annular bright-field (LAADF)-STEM imaging and electron energy loss spectroscopy (EELS) measurements also confirmed higher decomposition temperature and slow dynamic transformation process of deposited $NiCl_2.6H_2O$ on GO nanosheets in the solid state during heating compared to a-C substrate (Figures S7, S8, Supporting Information).

Based on SAED, EELS, and HR-TEM findings, we speculate that slower thermolysis kinetics of nickel salt on GO substrate compared to a-C originated from intrinsic features of GO, including 1) High density of oxygen functional groups. GO contains a large number of oxygen functional groups (such as hydroxyl, carboxyl, and epoxy groups) on its surface, making the surface more hydrophilic and polar. These functional groups can interact with other molecules, including Ni and Cl atoms, and hinder their movement on the surface. 2) Presence of defects and disordered structure. GO is a highly disordered material with many defects, such as vacancies, wrinkles, and edges. These defects can trap atoms and impede their diffusion across the surface. 3) Weak Van der Waals Interactions. The interactions between GO layers are weak van der Waals forces, which are relatively weak compared to other types of intermolecular forces. As a result, the layers can slide or rotate relative to each other, making it difficult for atoms to move across the surface. 4) Hindered molecular crowding. The surface of GO is crowded with molecules and atoms (functional groups, defects), which can restrict the movement of other atoms on the surface. This molecular crowding effect can be particularly

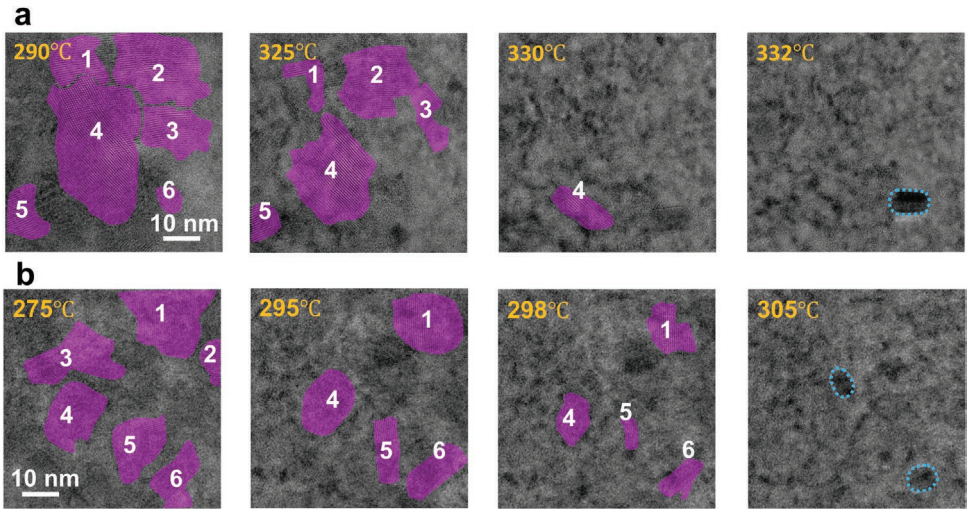

Figure 4. Sequential HR-TEM images illustrating the evolution of $NiCl_2.6H_2O$ into Ni nanoparticles upon thermolysis on a) GO and b) a-C. The regions in purple highlight nickel chloride crystallites shrinking with temperature, and the cyan counter lines indicate the edge of the newly formed Ni nanoparticles.

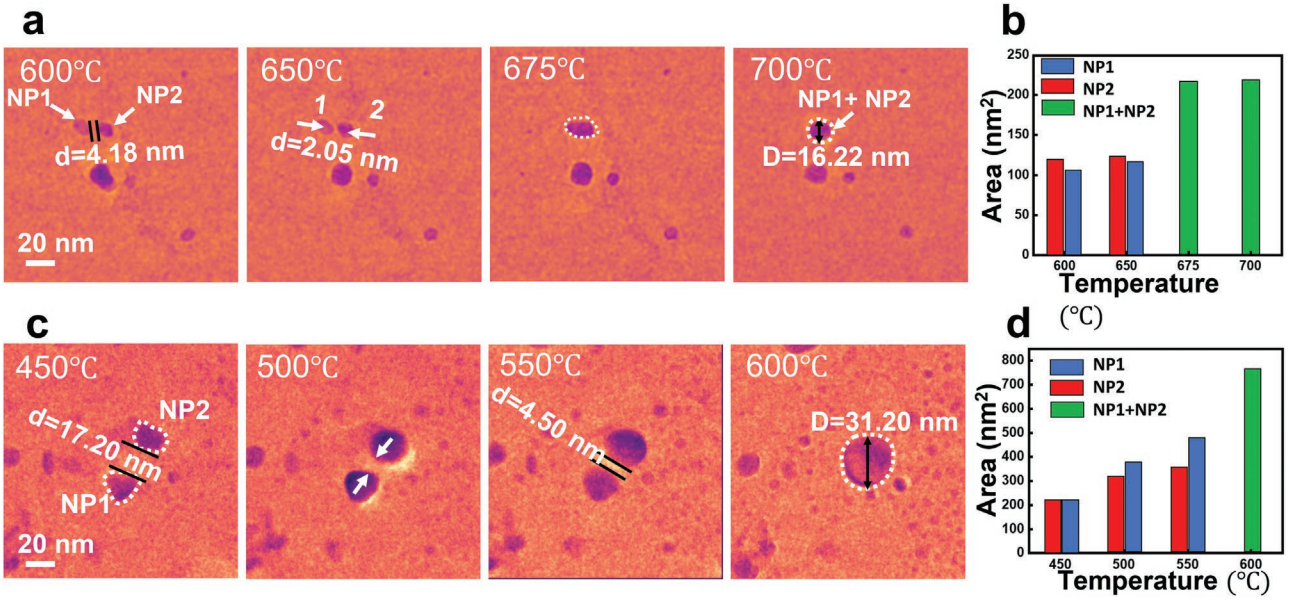

Figure 5. in situ temperature-resolved TEM image series illustrating the coalescence of Ni nanoparticles during heating. a) The coalescence of Ni NP1 and NP2 on GO, and b) the corresponding projected area of NP1 and NP2 as a function of temperature. c) The coalescence of Ni NP1 and NP2 on amorphous carbon (a-C). d) The corresponding particle area of NP1 and NP2 as a function of temperature.

strong in areas with high oxygen functional groups or defect concentrations.

Furthermore, we observed that extended exposure of nanoparticles to high temperatures favors gradual agglomeration and coalescence of NPs at the nanoscale that depends on the substrate. As shown in **Figure 5**a, the two small nanoparticles (NP1, NP2) formed on rGO via heating have an interparticle distance of 4.18 nm at 600 °C. By increasing the temperature to 650 °C, two NPs migrated toward each other at a close distance of 2.05 nm while their size did not change (Figure 5b). The two NPs attached at 675 °C and formed a larger nanoparticle with an average diameter of 16.22 nm. This observation indicates that coalescence is the driving force for particle growth on the rGO substrate during heating when the interparticle distance is small. Additionally, we tracked the migration and attachment of nanoparticles with temperature during heating on a-C support. As shown in Figure 5c, the two isolated NP1 and NP2 are 17.20 nm apart at 450 °C, which is significantly larger compared to the case we discussed for rGO. The distance between these two NPs decreased with the increase in temperature to 4.50 nm at 550 °C. Finally, the coalescence of NPs 1 and 2 produced a new particle with an average diameter of 31.20 nm. The change in the particle area of the corresponding NPs is presented in Figure 5d. We notice that the size of NP1 and NP2 increased slightly with temperature (450–550 °C), which might be due to the direct attachment of available Ni atoms on the a-C surface. Finally, the jump in particle area coincided with the coalescence of NP1 and NP2 at (600 °C) and formed a new particle with a spherical shape (NP1 + NP2). Therefore, the long-distance migration and coalescence of the formed NPs on a-C compared to rGO support highlight the stronger Ni NP-rGO interaction than Ni NP-amorphous carbon.

Moreover, we tracked the size of NPs formed on rGO and a-C with temperature to gain more insight into the governing particle growth mechanisms and their thermal stability (**Figure 6**). As shown in Figure 6a,b, we labeled five NPs on rGO and measured their corresponding particle area evolution with temperature. The inter-particle distance from each other and their positions almost remained unchanged at the 600–750 °C temperature range, which featured higher thermal stability of NPs formed on rGO. In the meantime, we observed a slight fluctuation uptrend in the measured surface area of NPs marked as 1, 3, and 5. The particle size of NP4 enlarged and NP2 reduced with the increase in temperature, suggesting Ni atoms attachment and/or Ostwald ripening growth pathways. Compared with the rGO substrate, the formed NPs on a-C showcased a size change that began at a lower temperature (Figure 6c,d). During the temperature-lapsed TEM imaging, we observed inapparent position movements of seven labeled NPs. Furthermore, the surface area of small NPs marked as 2,3,4,5,7 continued to reduce as a function of temperature while a large particle marked as NP1 increased in size. This phenomenon was in accordance with the Ostwald ripening growth model in which mass transport/atom diffusion occurs between immobile nanoparticles and large particles grow at the expense of small ones.[27] Figure S9a,b (Supporting Information) shows particle size distribution analyses of the synthesized nanoparticles on rGO and a-C substrates during heating and cooling treatment. The majority of nanoparticles with a diameter less than 10 nm and an average size of 7.62 nm formed on rGO. In comparison, we observed nanoparticles with nearly bimodal size distribution (25 and 60 nm) with a mean diameter of 37.61 nm formed on a-C support.

Next, we evaluated the structural evolution of carbon substrates during exposure to high temperatures. The acquired SAED show diffused diffraction rings revealing the amorphous nature of the GO substrate before applying the heating cycle (**Figure 7**a). After heat treatment, the appearance of two sets of

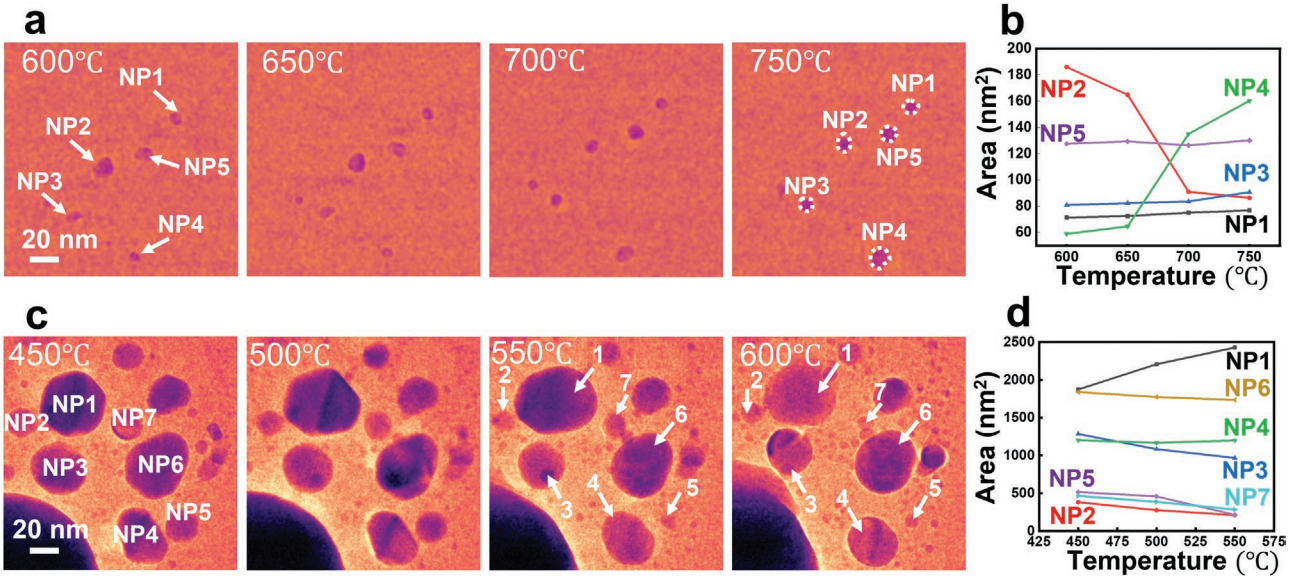

Figure 6. In situ temperature-resolved TEM image series depicting the Ni nanoparticles evolution during heating on a) rGO, five nanoparticles are labeled. b) Corresponding nanoparticles size change from 600 °C to 750 °C. c) amorphous carbon (a-C), seven nanoparticles highlighted. d) Corresponding nanoparticles size change from 450 to 600 °C.

hexagonal diffraction patterns indicates the structural transformation of GO (Figure 7b). The hexagonal patterns rotated by 13.5°, corresponding to a misorientation between two individual rGO sheets. These spots are consistent with $(1\bar{1}0)$ and $(2\bar{1}\bar{1})$ planes of hexagonal lattice rGO nanosheets.[28] This observation confirms the structural transformation of GO upon heating and possibly the reduction of GO to rGO[29] During the high-temperature synthesis process of Ni/rGO composite. Additionally, it is worth mentioning that the appearance of multiple hexagonal spots in the SAED pattern of rGO can also be attributed to the back folding of edges, intrinsic rotational stacking faults, or overlapping domains and domain boundaries with the disorientation of graphene layers.[30] Also, HR-TEM imaging in Figure 7c clearly confirmed the local crystallization of GO

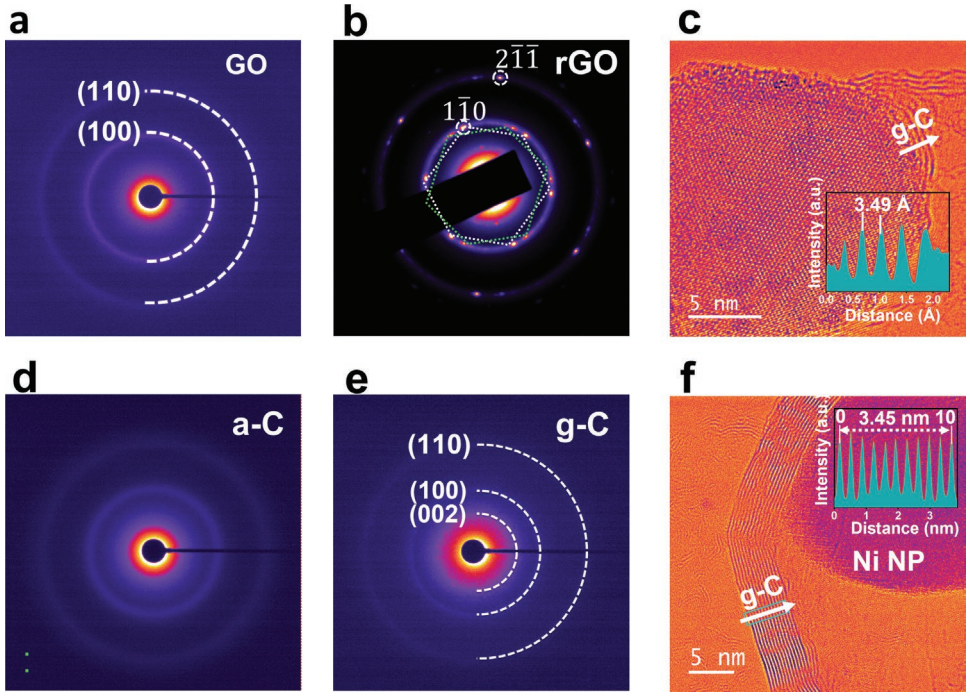

Figure 7. TEM characterization of GO and a-C transformation upon heating method. a,b) SAED patterns of GO nanosheets before and after heating, respectively. d,e) SAED patterns of a-C before and after slow heating, respectively. c,f) High magnification TEM images of crystalized carbon domains of rGO and a-C upon heat treatment, the averaged graphitic carbon (g-C) layer interplanar distance provided in the insets

domains upon heating treatment into a layered structure with an averaged interplanar spacing of 3.49 Å, consistent with the (002) plane of graphitic carbon (g-C).[31] Figure 7d shows faint diffused rings in the SAED pattern of a-C, indicating the amorphous nature of the carbon substrate. We also confirmed partial graphitization of a-C substrate at elevated temperature upon heat treatment, as shown with sharp rings in Figure 5e, indicating improved crystallinity. The diffraction rings which demonstrate numerous orientations with measured interplanar-spacing of these rings 3.42, 2.12, and 1.23 Å are corresponding to (002), (100) and (110) interlayer planes of graphite (P63/mmc; $a = b = 2.470$ Å, $c = 6.724$ Å; JCPDS 41–1487), respectively.[20,32,33] HR-TEM image of both long-range multilayer graphitic region ($d = 3.45$ Å) and short-range ordered carbon rearrangements of crystallized a-C after the heating program is shown in Figure 7f. HR-TEM imaging confirmed that graphitic (001) planes formed at the Ni-carbon interface on both rGO and a-C support. Compared to GO support, a thicker graphitic shell (>10 layers) formed using a-C substrate due to a more available carbon source for Ni catalytic graphitization (Figure 7c,f).

The solid-state transformation of amorphous carbon support into graphitic carbon (g-C) has been reported at elevated temperatures. For example, the complete transformation of amorphous carbon (a-C) into graphite without a catalyst requires high temperatures of ≈2000–3000 °C and proceeds via various intermediate states.[34,35] However, a-C in contact with reactive metallic catalysts (e.g., Fe, Co, Ni) crystallizes into graphitic carbon at lower temperatures (<1000 °C), which is known as catalytic graphitization.[36–40] Three well-established mechanisms of carbon dissolution-precipitation, metal-mediated or metal-induced crystallization (MMC and MIC), and metal-enhanced surface diffusion are proposed for this solid-state transformation process.[35]

Graphitization affects metal nanoparticles' growth, stability, and ripening at higher temperatures. The observed differences in nanoparticles migration and coalescence at higher temperatures can be explained via the following mechanisms: 1) The higher degree of graphitization in a-C (Figure S10, Supporting Information) can lead to more intense graphitic (001) planes formation where the bonding between Ni and (001) planes are weak.[41] Such weaker anchoring of Ni onto the (001) basal plane of graphitic carbon facilitates the movement of Ni aggregates on a-C substrate at high temperatures. Such weak bonding is also shown for other metallic nanoparticles, such as Pt nanoparticles and the (001) basal plane of graphene.[20] 2) The encapsulated Ni NPs can experience higher pressure as the number of graphitic layers increases, as observed for graphitization of the a-C substrate.[42] As a thick graphitic shell formed around Ni NPs using a-C support, part of the Ni particle is forced to flow away from the weakest sites of the graphitic encapsulation (Figure S10b, Supporting Information). Subsequently, a higher degree of metal flow on a-C substrate statistically would increase the possibility for collision and formation of larger NPs. A similar observation by Anton,[41] demonstrated that Ni particles encapsulated with graphite shells upon sequential inward nucleation of graphene layers at the metal-graphite interface. Eventually, the pressure on the metal core builds up, and the Ni is forced to expel and spread on the a-C substrate. 3) The higher stability of Ni NPs on rGO compared to a-C can also be correlated to higher defective sites, remaining oxygen functional groups, and edge plane content in rGO. These functional groups can form strong bonding with particles. It is reported that during the thermal reduction of GO, functional groups including epoxide, carbonyl, and ether could be removed from the GO at temperatures below 900 C, while hydroxyl groups are stable up to 900–1200 °C.[43] Considering the temperature range of our experiments, we believe there are some remaining hydroxyl groups on the rGO surface that strongly interact with Ni NPs resulting in their stabilization. Furthermore, as shown in Figure S10a (Supporting Information), Ni NPs are distributed in defective sites or edge planes of rGO. This could be attributed to the covalent bonding of Ni with the edge planes of rGO. Similarly, the Pt particle formed covalent bonding with the graphene edge plane, which provides more stability to the particles than the basal plane.[20] In contrast, the lack of functional groups and the abundance of graphite (001) planes present in the a-C substrate are expected to lead to the migration and coalescence of Ni NPs.

Upon heat treatment, the rGO substrate is decorated with cubic phase Ni nanoparticles depicting sharp contrast and spherical morphology, as shown in **Figure 8**a. The electron diffraction pattern of the NPs anchored to the surface of rGO reveals diffraction rings that are well matched to the (111), (200), (220), and (311) planes of thermodynamically stable face-centered cubic Ni (*fcc*-Ni, space group: $Fm\bar{3}m$) phase (Figure 8b). The lattice constant calculated based on the radii of diffraction rings is estimated to be $\alpha = 3.58$ Å. Atomic resolution high-angle annular bright-field (HAADF)-STEM image of a Ni nanoparticle (Figure 8c) shows the single crystalline nature of the Ni nanoparticles with a resolved lattice spacing of 2.07 and 1.79 Å (marked with yellow lines) assigned to the (111) and (200) family planes of *fcc*-Ni, respectively. In addition, the atomic model with white circles representing Ni atoms matched perfectly with the Ni positions. Examining the 2D fast Fourier transform (FFT) of the Ni nanoparticle shown in the inset image indicates cubic arrangement along <110> zone axis. The correlation of (002) and (020) planes with a *d*-spacing of 2.07 Å and angles between them indicate *fcc*-Ni at <100> orientation. The superimposed atomic model and FFT in the inset coincide well with Ni columns at this zone axis.

Upon heating/cooling treatment, NPs with nonuniform size and cubic crystal structure formed on a-C. The low-magnified HAADF-STEM in Figure 8d depicts randomly shaped NPs with high contrast after heat treatment. The SAED pattern in Figure 8e presents two sets of diffractions. One marked with a red semicircle with a measured interplanar spacing of 3.42 Å matched (002) plane of graphitic carbon, which means the partial transformation of amorphous carbon substrate into graphitic carbon (g-C). As mentioned above, this can be due to Ni catalytic graphitization of amorphous carbon via carbon dissolution (carburization)-precipitation mechanisms below 800 °C.[35,44,45] The other four sharp polycrystalline diffraction rings highlighted with white semicircles in Figure 8f matched well with the *fcc*-Ni phase. Figure 8f represents a high-resolution HAADF-STEM image and corresponding FFT pattern, which correspond with *fcc*-Ni along the (112) zone axis. The d-spacing of 2.07 Å correlates to the (002) plane of the cubic Ni phase.

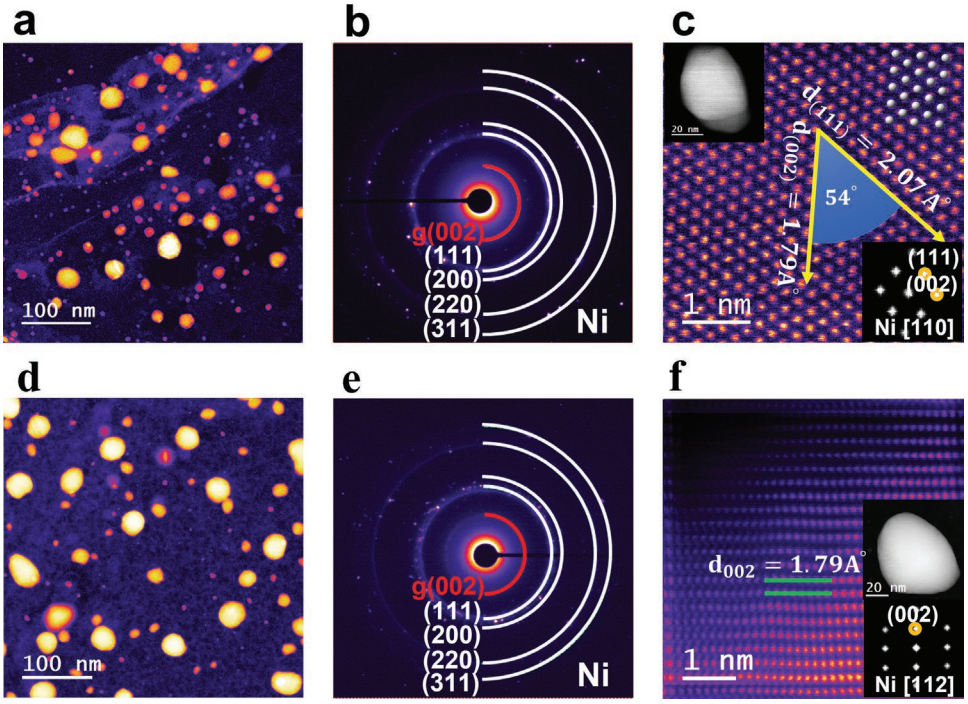

Figure 8. Atomic resolution characterization of Ni NPs formed on rGO and amorphous carbon via heating. a) Low magnification TEM image of Ni NPs/rGO hybrid after heating/cooling process at room temperature. b) SAED pattern of Ni/rGO demonstrating hybrid graphene/amorphous carbon (g/a-C) supported *fcc*-Ni crystal phase. c) Atomic resolution HAADF-STEM image of *fcc*-Ni NP along (110) zone axis, the particle, and FFT shown in the inset. The matching atomic model associated with {002} and {111} family planes is highlighted. d) Low-magnification HAADF-STEM image of Ni NPs/a-C after heating/cooling treatment. e) SAED pattern of Ni/a-C confirming *fcc*-Ni crystal phase and partial graphitization of amorphous carbon. f) Atomic resolution HAADF-STEM image of *fcc*-Ni NP crystal viewed along the (112) zone axis, inset shows the corresponding particle and FFT

The formation of a stable *fcc*-Ni phase upon heating can be explained by the Gibbs free energy minimization concept. The prolonged high-temperature exposure provides structural relaxation through atomic rearrangement/ordering. As such, Ni atoms have adequate time to rearrange to their thermodynamic equilibrium phase of *fcc*-Ni.[46] This favors the equilibrium state of NPs with the lowest free energy phase.[47,48]

It is worth highlighting that in our study, we did not observe the size effect dependency of the crystal structure of Ni nanoparticles. In fact, the Ni nanoparticles with average diameters of 7.62 and 37.62 nm on rGO and a-C, respectively, both show the *fcc* phase. In general, Ni can crystallize to thermodynamically stable *fcc* and metastable hexagonally close-packed (*hcp*) phases with relatively close bulk energy.[49] The bulk energy difference per atom between the *fcc* and Ni phases, ΔE_B(*fcc*–*hcp*) = −28 meV atom^{-1}, indicates *fcc* crystal structure is energetically more favorable at ambient conditions.[50,49] However, an early work by Illy et al.[51] found that the Ni nanoparticle crystal phase is size dependent. They observed that Ni nanoparticles smaller than ≈4 nm demonstrated *hcp* crystal while the larger particles showed *fcc* structure. Later, Tzitzios et al.[52] synthesized nano-sized *hcp*-Ni particles with sizes ranging from 13 to 25 nm. One possible explanation for the size effect in the crystal structure is the surface energy contribution term to the overall energy of the nanoparticle, which increases with the size reduction. This in turn facilitates the formation and stabilization of the metastable phase of nanocrystal structures.[53] Furthermore, Tian et al.[54] reported *hcp*-Ni nanostructures stabilized in small crystallite sizes (up to ≈5 nm) by heteroepitaxial growth on the (001) plane of MgO. They correlated this observation to the reduction of misfit strain energy between the *hcp*-Ni structure and the (001) face of MgO.

STEM-EELS and STEM-energy-dispersive X-ray spectroscopy (STEM-EDS) confirmed the chemistry and compositional distribution of the as-synthesized NPs on rGO nanosheets and a-C as nickel nanoparticles (Figures S11, S12, Supporting Information). Additionally, our chemical analyses (EELS and EDS) ruled out the formation of any Ni-carbide or Ni-oxide compounds upon the heating cycle. The carbide formation can happen during the heating process of carbon materials in the presence of catalytic active metals.[40] It has been reported that the carbide compounds might act as stable or as an intermediate product.[41] However, it is shown that carbide compounds can become unstable and decompose into graphite and metals at elevated temperatures.[36,55] In our experimental conditions which the temperature is far above the thermal decomposition of Ni-carbide (500 °C), no intermediate Ni-carbide was identified.[41]

In order to shed light on the mechanism of Ni NP formation over GO and amorphous C, the density functional theory (DFT) calculations of $NiCl_2$ decomposition are performed. It is observed experimentally that the $NiCl_2$ decomposition reaction rate is different over the GO and a-C surfaces. Specifically, $NiCl_2$ decomposition over the GO surface is delayed compared to the a-C by 15 °C (cf. Figures 3, 4). We have performed a series of ab-initio calculations to understand better the mechanism

behind such temperature delay. First, GO and a-C slabs were created (cf. Figure S13, Supporting Information) and optimized following our previous work.[56] Several configurations of GO and a-C varying defects and OH groups location were considered. The ground-state energy of each such structure is very similar as long as the atomic percentage is preserved. Thus, one representative sheet of GO and a-C was chosen for DFT calculations. In the second step, various $NiCl_2$ positions over the identified GO and a-C surfaces to find the most favorable atomic configuration of GO/$NiCl_2$ and a-C/$NiCl_2$ were considered, followed by the nudge elastic band (NEB) calculations to reveal the energy barrier of Cl_2 release. Since, the Cl_2 release leads to the formation of pure Ni over a corresponding surface, this is considered to be a first step in the formation of Ni NP as observed experimentally.

We have considered two configurations with two and four $NiCl_2$ molecules for each structure. These cases represent low and high $NiCl_2$ coverage over the GO and a-C surface. We first studied Cl_2 formation and desorption from the GO, followed up by the a-C. **Figure 9**a,c illustrate the path (left-hand images) and energetics (right-hand images) of Cl_2 removal from the GO and a-C surface in the presence of two $NiCl_2$ molecules (a low coverage case), correspondingly. The binding energy of the resulting structures is lower than the initial configuration with Cl_2 at the surface, indicating that the formation of Ni clusters at the surface of the GO and a-C is favorable. However, the binding energy only indicates the thermodynamic stability of a structure, kinetically, the vibration energy is the dominant factor of Cl_2 removal. Thus, we have performed a series of NEB calculations to evaluate activation energy for Cl_2 removal from the GO and a-C surfaces. The right-hand images in Figure 9a,c show the calculated barriers for Cl_2 desorption. The process of Cl_2 desorption from the GO surface is kinetically unfavorable by 2.61 eV. A similar situation is observed for Cl_2 desorption from the a-C (Figure 9b, right-hand side), where the activation energy of 1.99 eV was obtained in DFT calculations. Analyzing the kinetics of Cl_2 removal from the GO and a-C surfaces obtained in DFT calculations, it could be concluded that none of these processes proceed spontaneously, even at elevated temperatures, as observed in the experiment. Following experimental results (cf. Figure 4), it could be observed that the surface $NiCl_2$ coverage is significant, which could result in active interaction among $NiCl_2$ molecules. This could change the stability of adsorbates leading to more kinetically favorable Cl_2 removal. To evaluate the influence of other $NiCl_2$ molecules on Cl_2 removal energetics, the number of $NiCl_2$ was increased to four for both surfaces. The ab-initio molecular dynamics (AIMD) simulations for 1000 fs at 290 °C for the GO and 275 °C for a-C in the presence of four $NiCl_2$ molecules were performed. These two temperature points correspond to the beginning of $NiCl_2$ decomposition, as revealed by our experimental measurements (cf. Figure 3). The AIMD simulations show a significant bond stretching for all Ni—Cl bonds (cf. Figure S14, Supporting Information), indicating that at elevated temperatures with high $NiCl_2$ coverage Cl_2 removal becomes energetically more feasible. Correspondingly, using configurations obtained in the AIMD simulations after 1000 fs, the thermodynamic and kinetic stability of the resulting structures is calculated by the DFT. Similarly, as for the case of two $NiCl_2$ molecules, thermodynamically, the removal of Cl_2 is favorable, leading to the enthalpy change of ≈–0.6 eV (Figure 9b,d). However, kinetically, this process is significantly more favorable than the Cl_2 removal in the presence of two $NiCl_2$ molecules (Figure 9a,c). In particular, the activation barrier for Cl_2 removal from the GO in the presence of four $NiCl_2$ molecules is reduced to 1.4 eV, and for a-C surface to 1.12 eV, compared to the corresponding cases of two $NiCl_2$ molecules. This indicates that the formation of Ni clusters over the GO and a-C surface for high $NiCl_2$ coverage is

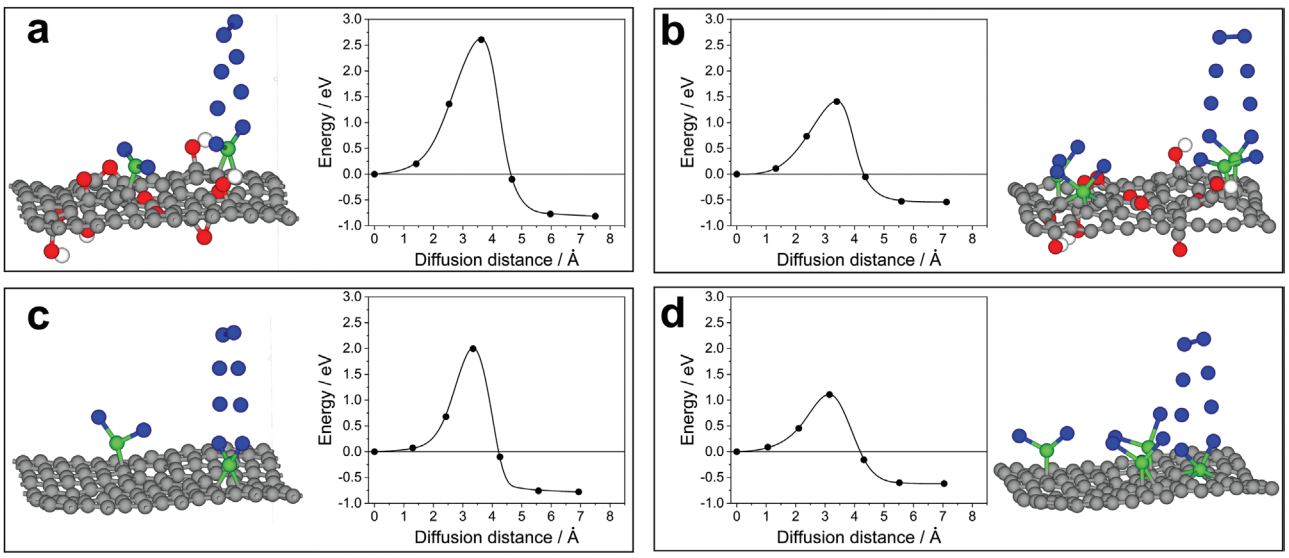

Figure 9. DFT calculation results of Cl_2 removal from GO and a-C surface leading to the formation of Ni clusters. a,b) illustrate Cl_2 desorption from the GO surface in the presence of two and four $NiCl_2$ molecules, correspondingly. c,d) show Cl_2 removal from the a-C surface for two and four $NiCl_2$ molecules, respectively. For all pictures, the molecular schematic depicts the path of Cl_2 removal, and the graph shows the energetics. The grey spheres represent carbon atoms, the red spheres are oxygen atoms, the white spheres are hydrogen atoms, the green spheres are Ni atoms, and the blue spheres depict chlorine atoms.

plausible at elevated temperatures, as observed in the present experimental measurements.

3. Conclusion

In summary, Ni nanoparticle formation based on thermolysis reaction enabled by heating treatment on rGO and hybrid graphitic/amorphous carbon (g/a-C) was investigated using an in situ TEM. The Ni salt underwent a multistep process including thermal decomposition of Ni salt precursor, reduction at high temperature, and crystal growth to nanoparticles. Nickel chloride decomposition occurs at higher temperatures with slower kinetics on GO nanosheets than on a-C substrate. This could be due to strong Ni interaction with GO, high-density oxygen functional groups, defects, Weak Van der Waals, and hindered molecular crowding properties of GO nanosheets. The DFT calculations and AIMD simulations provided molecular-level evidence of facilitating Ni cluster formation for higher $NiCl_2$ coverage. Moreover, the higher temperature and slow decomposition kinetics of $NiCl_2$ on the GO surface is closely related to the higher activation barrier for Cl_2 removal using GO substrate compared to the a-C surface. We observed that carbon substrate graphitization during heating significantly impacted nanoparticle evolution. Moreover, the Ni particles formed on rGO showed 500% smaller average sizes. Ni nanoparticles migration and coalescence were facilitated on a-C support compared to rGO. In contrast, small Ni NPs with high thermal stability formed on rGO. Furthermore, we found that the minimum distance between Ni NPs before coalescence on a-C was four times larger than in the case of rGO. We suggest the better thermal stability of Ni NPs on rGO is due to strong interaction with edge defects and functional groups in the GO surface. Furthermore, graphitic carbon encapsulation and expelling of Ni facilitated particle growth on an a-C substrate. Additionally, our findings indicate that thermolysis results in thermodynamically stable *fcc*-Ni phase formation on rGO and a-C, independent of the size of Ni NPs. Reveling the pathways of metal salt decomposition on various carbon substrates is expected to yield better design metal-carbon heterostructures for catalysis, sensing and electronics, and filters.

4. Experimental Section

Sample Preparation: Nickel (II) chloride hexahydrate ($NiCl_2{\cdot}6H_2O$, ≥99%) and absolute ethanol were purchased from Sigma Aldrich, which were used as received for sample preparation. The monolayer GO was prepared using modified hummer's approach with a disorder band to graphite lattice band (D/G) of 0.86 and carbon to oxygen ratio C/O of ≈3.5 in the structure.[57] Homogenous nickel chloride solution was prepared by dissolving $NiCl_2{\cdot}6H_2O$ (20 mmol) in the ethanol solution via magnetic stirring for 1 hr at 600 rpm and subsequent bath sonication for 10 min. GO suspension (0.1 ml) was diluted in ethanol (4 ml) and sonicated for 10 min to ensure good dispersion of GO nanosheets. Then, Ni salt solution and diluted GO suspension (0.1 mg ml^{-1}) were mixed (1:1). The final mixture experienced combinations of vortex mix and sonication for 10 min each to obtain a uniformly dispersed sample. Next, 1 µl of the associated samples were drop-cast onto Protochips Fusion thermal chips membrane-supported holey carbon films for in situ experiments. For in situ synthesis of Ni NPs on amorphous carbon, the same concentration of nickel salt solution was just directly dropped cast onto the supported lacy carbon of the heating chip. Afterward, the dedicated Fusion Select double title heating holder was loaded into the microscope to run heating/cooling experiments with temperature accuracy over 95% for TEM analysis. The annealing of Ni precursor on GO and amorphous carbon (a-C) was followed heating/cooling in which the initial samples were heated to 1100 °C at a ramp rate of 10 °C min^{-1}. Subsequently, it cooled down to room temperature (25 °C) at 10 °C min^{-1}.

TEM Characterization: The dynamic microstructure and morphology evolution of the experiments via in situ TEM and their crystal and chemical analyses at room temperature were performed using a spherical probe aberration-corrected JEOL TEM/STEM ARM 200CF equipped with a cold field emission gun at 200 kV using. The HAADF, LAADF, and Annular bright field detectors with 40, 90, and 23 mrad detector collection angles, respectively, were used to acquire STEM micrographs. A 22 mrad probe convergence semi-angle was used to perform STEM imaging with an Orius CCD camera and frame sizes of 512 × 512 pixels. Moreover, A JEOL JEM-3010 transmission electron microscope operated at 300 keV was utilized to obtain SAED micrographs of rGO and Ni/rGO samples by using the TEM diffraction mode. The constant electron diffraction camera length (20 cm) and selected area aperture were utilized for comparative purposes of in situ heating experiments. S/TEM images and SAED micrographs were processed using Digital Micrograph (Gatan Inc.). To perform chemical analysis, STEM-EDS data, including elemental spectrum and mappings collected via an Oxford Xmax 100TLE windowless X-ray detector.

The EELS signal collected with a Gatan imaging filter with a camera length of 20 mm and probe size 6C with 0.15, 0.3, and 0.75 eV of energy dispersion per channel, depended on the required energy range using an aperture of 2.5 mm with a collection semi-angle β of 41.7 mrad and beam current of 15.4 pA on a JEOL 200CF ARM microscope operating at 200 kV. The EELS data was obtained using the dual-EELS technique to simultaneously acquire the core-loss and low-loss spectra. The EELS spectrum for the core-loss spectra was processed using Origin Pro software after power law background and continuum subtraction performed in the Gatan Digital Micrograph software (V 3.4). The L_3/L_2 integrated intensity ratios were measured using D.R.G. Mitchell's 'double arctan EELS background' script (2015) in Gatan Digital Micrograph software (V 3.4) to remove continuum background in the EELS signal and using integration windows (8 eV width) centered on the peaks.[58] Afterward, the oxidation state of Ni during the metal salt thermolysis process was determined by comparing the L_3/L_2 integrated intensity ratios at different temperatures. The low-loss region was used to determine the relative sample thickness (t/λ), where t is the average thickness of the investigated region of interest and λ is the inelastic mean free path of the electrons. This value was smaller than 0.4 to collect EELS data with a good signal-to-noise ratio and minimize scattering events.

EFTEM was performed to obtain the elemental maps of Cl, O, and Ni. The edge position of each element (Cl L-edge, O K-edge, and Ni $L_{2,3}$ edge of Ni were determined by EELS in advance. The maps were acquired for Cl–L (slit width: 20 eV, pre-edge 1: 168 eV, pre-edge 2: 188 eV, post-edge: 210 eV), O–K (slit width: 30 eV, pre-edge 1: 484 eV, pre-edge 2: 514 eV, post-edge: 547 eV) and Ni–$L_{2,3}$ (slit width: 40 eV, pre-edge 1: 790.7 eV, pre-edge 2: 830.7 eV, post-edge: 874.7 eV) edges using the three-window method to extract the core-loss information, and were presented in pseudocolor: Ni (yellow), Cl (red) and O (blue). Other than recording images, the electron beam blanked to avoid undesired beam-induced effects during thermal treatment experiments.

Computational Methods: DFT calculations and AIMD simulations

The DFT calculations were performed using Vienna Ab Initio Simulations Package (VASP) code employing the generalized-gradient approximation[59] and the PBE (Perdew, Burke, and Ernzerhof)[60] functional for the exchange-correlation effects. For systems with an odd number of electrons, non-spin-polarized calculations, and for systems with even numbers of electrons spin-polarized calculations, were carried out. Cl_2 molecules migration paths and kinetic barriers were calculated

using the linear NEB method as implemented in the VASP code. A cutoff energy of 450 eV was used for all calculations as the optimal trade between the time of calculations and precision. All structural optimizations were carried out until the forces acting on atoms were below 0.01 eV $Å^{-1}$. The criterion for energy change was set to 0.1 meV. AIMD simulations were performed for 1000 fs with a 1 fs time step using the Nose-Hoover chain thermostat in the NVT ensemble. All atomic structures and slabs were created using the Atomistic Tool Kit.[61]

Supporting Information

Supporting Information is available from the Wiley Online Library or from the author.

Acknowledgements

R.S.-Y. is thankful to National Science Foundation (NSF) for award number DMR-1809439. The present work made use of the JEOL JEM-ARM200CF in the Electron Microscopy Service of the Research Resources Center, RRC, at the University of Illinois at Chicago (UIC). V.Y. acknowledges the financial support from NSF award number DMR-2055442.

Conflict of Interest

The authors declare no conflict of interest.

Data Availability Statement

The data that support the findings of this study are available from the corresponding author upon reasonable request.

Keywords

ab-initio calculations, in situ transmission electron microscopy, nickel nanoparticles, thermolysis

Received: November 25, 2022
Revised: March 16, 2023
Published online: April 23, 2023

[1] Y. Yin, A. P. Alivisatos, *Nature* **2005**, *437*, 664.
[2] I. E. Uflyand, G. I. Dzhardimalieva, *Nanomaterials Preparation by Thermolysis of Metal Chelates*, Springer, Cham **2018**.
[3] A. K. Tyagi, R. S. Ningthoujam, *Handbook on Synthesis Strategies for Advanced Materials*, Springer, Singapore **2021**.
[4] C. Wu, D. Xie, Y. Mei, Z. Xiu, K. M. Poduska, D. Li, B. Xu, D. Sun, *Phys. Chem. Chem. Phys.* **2019**, *21*, 17571.
[5] C. Al, O. S. Co, S. M. Kim, W. Liao, A. M. Kierzkowska, T. Margossian, D. Hosseini, S. Yoon, M. Broda, C. Cope, C. R. Mu, *Chem. Mater.* **2018**, *30*, 1344.
[6] J. Duan, L. Liu, Z. Wu, J. Fang, D. Chen, *CrystEngComm* **2018**, *20*, 4025.
[7] D. S. Gavhane, A. D. Sontakke, M. A. Van Huis, *Adv. Funct. Mater.* **2022**, *32*, 2106450.
[8] X. Sang, X. Li, A. A. Puretzky, D. B. Geohegan, K. Xiao, R. R. Unocic, *Adv. Funct. Mater.* **2019**, *29*, 1902149.
[9] L. Fei, S. Lei, W. Zhang, W. Lu, Z. Lin, C. H. Lam, Y. Chai, Y. Wang, *Nat. Commun.* **2016**, *7*, 12206.
[10] S. Park, K.-S. Lee, G. Bozoklu, W. Cai, S. T. Nguyen, R. S. Ruoff, *ACS Nano* **2008**, *2*, 572.
[11] X. Liu, R. Ma, X. Wang, Y. Ma, Y. Yang, L. Zhuang, S. Zhang, R. Jehan, J. Chen, X. Wang, *Environ. Pollut.* **2019**, *252*, 62.
[12] S. Z. N. Ahmad, W. N. Wan Salleh, A. F. Ismail, N. Yusof, M. Z. Mohd Yusop, F. Aziz, *Chemosphere* **2020**, *248*, 126008.
[13] J. P. Patterson, D. B. Collins, J. M. Michaud, J. L. Axson, C. M. Sultana, T. Moser, A. C. Dommer, J. Conner, V. H. Grassian, M. D. Stokes, G. B. Deane, J. E. Evans, M. D. Burkart, K. A. Prather, N. C. Gianneschi, *ACS Cent. Sci.* **2016**, *2*, 40.
[14] S. S. J. Aravind, V. Eswaraiah, S. Ramaprabhu, *J. Mater. Chem.* **2011**, *21*, 17094.
[15] M. K. King, M. K. Mahapatra, *Int. J. Thermophys.* **2022**, *43*, 32.
[16] S. Gao, S. Hao, Z. Huang, Y. Yuan, S. Han, L. Lei, X. Zhang, R. Shahbazian-Yassar, J. Lu, *Nat. Commun.* **2020**, *11*, 2016.
[17] Y. Shen, V. Boffa, I. Corazzari, A. Qiao, H. Tao, Y. Yue, *Carbon* **2018**, *138*, 337.
[18] A. V. Dolbin, M. V. Khlistyuck, V. B. Esel'Son, V. G. Gavrilko, N. A. Vinnikov, R. M. Basnukaeva, I. Maluenda, W. K. Maser, A. M. Benito, *Appl. Surf. Sci.* **2016**, *361*, 213.
[19] D. Appy, H. Lei, C.-Z. Wang, M. C. Tringides, D.-J. Liu, J. W. Evans, P. A. Thiel, *Prog. Surf. Sci.* **2014**, *89*, 219.
[20] Z. Huang, Y. Yao, Z. Pang, Y. Yuan, T. Li, K. He, X. Hu, J. Cheng, W. Yao, Y. Liu, A. Nie, S. Sharifi-Asl, M. Cheng, B. Song, K. Amine, J. Lu, T. Li, L. Hu, R. Shahbazian-Yassar, *Nat. Commun.* **2020**, *11*, 6373.
[21] A. Eremin, E. Gurentsov, *Mater. Chem. Phys.* **2019**, *228*, 180.
[22] K. K. Nanda, A. Maisels, F. E. Kruis, *J. Phys. Chem. C* **2008**, *112*, 13488.
[23] A. Van Teijlingen, S. A. Davis, S. R. Hall, *Nanoscale Adv.* **2020**, *2*, 2347.
[24] C. H. Wu, *J. Colloid Interface Sci.* **2007**, *311*, 338.
[25] C. Chen, X. Wang, *Ind. Eng. Chem. Res.* **2006**, *45*, 9144.
[26] L. Chaabane, E. Beyou, A. El Ghali, M. H. V. Baouab, *J. Hazard. Mater.* **2020**, *389*, 121839.
[27] Z. Ying, J. Diao, S. Wang, X. Cai, Y. Cai, H. Liu, N. Wang, *Diamond Relat. Mater.* **2021**, *120*, 108690.
[28] N. R. Wilson, P. A. Pandey, R. Beanland, R. J. Young, I. A. Kinloch, L. Gong, Z. Liu, K. Suenaga, J. P. Rourke, S. J. York, J. Sloan, *ACS Nano* **2009**, *3*, 2547.
[29] S. H. Dave, C. Gong, A. W. Robertson, J. H. Warner, J. C. Grossman, *ACS Nano* **2016**, *10*, 7515.
[30] J. H. Warner, M. H. Rümmeli, T. Gemming, B. Büchner, G. A. D. Briggs, *Nano Lett.* **2009**, *9*, 102.
[31] S. Singh, K. Rathi, K. Pal, *J. Alloys Compd.* **2018**, *740*, 436.
[32] C. Li, X. Zhang, K. Wang, X. Sun, G. Liu, J. Li, H. Tian, J. Li, Y. Ma, *Adv. Mater.* **2017**, *29*, 1604690.
[33] X. Glad, J. Gorry, M. S. Cha, A. Hamdan, *Sci. Rep.* **2021**, *11*, 7516.
[34] J. N. Rouzaud, A. Oberlin, *Carbon.* **1989**, *27*, 517.
[35] D. Janke, F. Munnik, J. Julin, R. Hübner, J. Grenzer, C. Wüstefeld, S. Gemming, D. Rafaja, M. Krause, *Carbon* **2020**, *159*, 656.
[36] J. A. Rodríguez-Manzo, C. Pham-Huu, F. Banhart, *ACS Nano* **2011**, *5*, 1529.
[37] R. Lamber, N. Jaeger, G. Schulz-Ekloff, *Surf. Sci.* **1988**, *197*, 402.
[38] A. Ōya, H. Marsh, *J. Mater. Sci.* **1982**, *17*, 309.
[39] X. Yao, Y. Wei, Z. Wang, L. Gan, *ACS Catal.* **2020**, *10*, 7381.
[40] L. Gan, S. Rudi, C. Cui, P. Strasser, *ChemCatChem* **2013**, *5*, 2691.
[41] R. Anton, *Carbon* **2008**, *46*, 656.
[42] J. Y. Huang, *Nano Lett.* **2007**, *7*, 2335.
[43] M. Pelaez-Fernandez, A. Bermejo, A. M. Benito, W. K. Maser, R. Arenal, *Carbon* **2021**, *178*, 477.
[44] R. Sinclair, T. Itoh, R. Chin, *Microsc. Microanal.* **2002**, *8*, 288.
[45] S. Esconjauregui, C. M. Whelan, K. Maex, *Carbon* **2009**, *47*, 659.
[46] P. Motamedi, K. Bosnick, K. Cui, K. Cadien, J. D. Hogan, *ACS Appl. Mater. Interfaces* **2017**, *9*, 24722.

[47] F. Bai, K. Bian, X. Huang, Z. Wang, H. Fan, *Chem. Rev.* **2019**, *119*, 7673.
[48] T. D. Nguyen, C. C. Nguyen, V. H. Tran, *RSC Adv.* **2017**, *7*, 25406.
[49] H. Lin, J.-X. Liu, H. Fan, W.-X. Li, *J. Phys. Chem. C* **2020**, *124*, 11005.
[50] S. Schönecker, X. Li, M. Richter, L. Vitos, *Phys. Rev. B* **2018**, *97*, 224305.
[51] S. Illy, O. Tillement, F. Machizaud, J. M. Dubois, F. Massicot, Y. Fort, J. Ghanbaja, *Philos. Mag. A* **1999**, *79*, 1021.
[52] V. Tzitzios, G. Basina, M. Gjoka, V. Alexandrakis, V. Georgakilas, D. Niarchos, N. Boukos, D. Petridis, *Nanotechnology* **2006**, *17*, 3750.
[53] J. Liang, F. Ma, S. Hwang, X. Wang, J. Sokolowski, Q. Li, G. Wu, D. Su, *Joule* **2019**, *3*, 956.
[54] W. Tian, H. P. Sun, X. Q. Pan, J. H. Yu, M. Yeadon, C. B. Boothroyd, Y. P. Feng, R. A. Lukaszew, R. Clarke, *Appl. Phys. Lett.* **2005**, *86*, 131915.
[55] R. Anton, *Carbon* **2009**, *47*, 856.
[56] T. Foroozan, V. Yurkiv, S. Sharifi-Asl, R. Rojaee, F. Mashayek, R. Shahbazian-Yassar, *ACS Appl. Mater. Interfaces* **2019**, *11*, 44077.
[57] T. Foroozan, F. A. Soto, V. Yurkiv, S. Sharifi-Asl, R. Deivanayagam, Z. Huang, R. Rojaee, F. Mashayek, P. B. Balbuena, R. Shahbazian-Yassar, *Adv. Funct. Mater.* **2018**, *28*, 1705917.
[58] D. R. G. Mitchell, *Double Atan EELS Background*, 20150402, v2.0, http://www.dmscripting.com/double_atan_eels_background.html.
[59] M. Itoh, H. Tanaka, Y. Watanabe, M. Udagawa, I. Sumita, *Phys. Rev. B* **1993**, *48*, 4978.
[60] J. P. Perdew, K. Burke, M. Ernzerhof, *Phys. Rev. Lett.* **1996**, *77*, 3865.
[61] S. Smidstrup, T. Markussen, P. Vancraeyveld, J. Wellendorff, J. Schneider, T. Gunst, B. Verstichel, D. Stradi, P. A. Khomyakov, U. G. Vej-Hansen, M. E. Lee, S. T. Chill, F. Rasmussen, G. Penazzi, F. Corsetti, A. Ojanperä, K. Jensen, M. L. N. Palsgaard, U. Martinez, A. Blom, M. Brandbyge, K. Stokbro, *J. Phys.: Condens. Matter* **2020**, *32*, 015901.